A novel Lagrangian approach for the stable numerical simulation of fault and fracture mechanics

Andrea Franceschini, Massimiliano Ferronato *, Carlo Janna, Pietro Teatini

Department of Civil, Environmental and Architectural Engineering, University of Padova, via Trieste 63, 35121 Padova, Italy

A B S T R A C T

The simulation of the mechanics of geological faults and fractures is of paramount importance in several applications, such as ensuring the safety of the underground storage of wastes and hydrocarbons or predicting the possible seismicity triggered by the production and injection of subsurface fluids. However, the stable numerical modeling of ground ruptures is still an open issue. The present work introduces a novel formulation based on the use of the Lagrange multipliers to prescribe the constraints on the contact surfaces. The variational formulation is modified in order to take into account the frictional work along the activated fault portion according to the principle of maximum plastic dissipation. The numerical model, developed in the framework of the Finite Element method, provides stable solutions with a fast convergence of the non-linear problem. The stabilizing properties of the proposed model are emphasized with the aid of a realistic numerical example dealing with the generation of ground fractures due to groundwater withdrawal in arid regions.

© 2016 Elsevier Inc. All rights reserved.

1. Introduction

The possible activation of pre-existing faults and the generation of new fractures in the subsurface may play a critical role in several fields of great social interest, such as the management and the exploitation of groundwater resources, especially in arid areas, the hydrocarbon recovery and storage, and the monitoring of the seismic activity in the Earth's crust. The most known and studied effect related to the exploitation of subsurface resources, either groundwater or hydrocarbons, is land subsidence, that is still an important challenge in several world sites, e.g., [1,2]. It has been observed that the effect of a deep fault activation on the surface deformation is often negligible [3], but it can be much more significant from other points of view. For instance, the sliding and/or opening of a fault can create preferential leakage paths for the pore fluid escape, causing a matter of great concern in the process of storing fluids and hydrocarbons underground, such as CO_2 [4–7] or natural gas [8,9]. Another important consequence is the possible damage, or even break, of the well casings, that generally brings significant economical and environmental losses [10,11]. However, the most challenging effect connected to a fault activation is the possible earthquake triggering. Earthquakes associated with the production and injection of fluids have been recently reported, e.g., [12–14], as well as with the wastewater disposal, e.g., [15,16]. Similar issues arise also in the development of unconventional hydrocarbon reservoirs, i.e., the so-called oil and gas shales, and in the groundwater withdrawal from arid and semi-arid regions. The production from shale reservoirs has recently experienced a dramatic increase thanks to the deployment of the "fracking" technology, which is based on the massive generation of fractures

---

due to the injection of dense fluids at high pressures. The use of this technique in densely populated areas has raised a large scientific debate on the possible connected environmental risks [17–19]. The over-exploitation of fresh aquifers in arid regions has caused the generation of significant ground fissures, that have been reported in many alluvial basins since the late '70s. Examples of such localized ruptures, which can be regarded as newly generated faults emerging to the ground surface, have been recorded in the South-Western part of the United States [20], the Libyan desert [21], China [22], and central Mexico [23].

Despite the growing interest in the prediction of the mechanics of faults, many issues still remain unsolved. A most important one is the capability of reliably simulate the mechanical behavior of a fault in a numerically stable way. The use of numerical models to predict the variation of the full stress tensor, the pore pressure and the related fault slip during the production and/or injection of subsurface fluids is of paramount importance to develop reliable computational tools for the efficient and safe management of underground resources. Currently, the simplest way to deal with faults in a geomechanical model consists of regarding them as a part of the continuous porous body characterized by a different rheological behavior [24–26]. This approach, however, has several limitations. The most significant ones concern the difficulty in representing in a reliable way the actual constitutive behavior of the fault and modeling the possible slip of the discontinuity surface. The latter aspect turns out to be particularly important when the model is used to predict the expected magnitude of the earthquake triggered by the fault activation. In fact, recent studies suggest the use of simple mathematical relationships for correlating the maximum magnitude of a seismic event to the sliding fault area and the average slippage [27,28]. Another numerical approach that makes easier the identification of the localized discontinuous displacement possibly arising along the fault is based on the introduction of interface frictional elements. Several formulations have been proposed starting from the original work by Goodman et al. [29], e.g., [3,30–34]. Most of the currently available numerical methods make use of the penalty approach to enforce the continuity of the displacement across the fault whenever the activation condition is not achieved. This method is largely used for the ease of implementation and the fact that it does not increase the number of unknowns of the problem, but the resulting stiffness matrix can be severely ill-conditioned, requiring the use of special solvers [35–37]. Moreover, such an ill-conditioning can cause severe difficulties in the convergence of the Newton-like scheme used for the solution of the non-linear problem, with oscillatory behaviors between two non-equilibrated configurations.

An effective alternative to the penalty method relies on the use of Lagrange multipliers to enforce the contact constraints over the fault surfaces, e.g., [38]. The main numerical drawback connected with this technique is the fact that the introduction of the multipliers increases the size of the discrete problem, that typically exhibits a saddle-point structure. The present work introduces a novel formulation for the stable numerical simulation of the fault and fracture mechanics with the aid of the Lagrange multipliers. The basic variational formulation is modified by adding the contribution of the frictional work along the activated fault portion, computed according to the "Principle of Maximum Plastic Dissipation" [39,40] which prescribes that the friction energy must be as large as possible. This formulation results in a non-symmetric generalized saddle-point Jacobian matrix that ensures a robust convergence of the non-linear problem. The paper is organized as follows. The basic principles governing the mechanics of faults are briefly reviewed and the continuous variational problem is formulated. The numerical model is then introduced in the framework of the Finite Element (FE) method, providing several implementation details. The proposed model is finally tested in a few numerical examples. The stabilizing property of the contribution due to the principle of maximum plastic dissipation is shown along with the non-linear convergence rate. A realistic example dealing with the generation of a ground fracture due to groundwater withdrawal closes the work.

2. Numerical modeling of fault mechanics

A geological fault or a ground fracture, generally termed fault in the sequel, can be ideally conceived as a discontinuity within a three-dimensional (3D) porous body consisting of a pair of friction surfaces in contact each other. Although other approaches are also possible, e.g., approximating a fault by a 3D thin volume with properties different from the surrounding [24], the model based on the use of contact surfaces is generally more appropriate for regional-scale simulations and for describing the possible fault activation with the inception of localized discontinuous displacements [3,34]. In this case, the mechanical behavior of faults can be described by using the concepts of contact mechanics.

Generally speaking, contact problems involve situations where portions of the boundary of one body come into contact with portions of the boundary of the same or another body. The contact is subject to specific restrictions, such as friction and the non-compenetrability of solid bodies, that are described by the governing constitutive law. Such a law can be very problem dependent, for a general overview see for instance [40,41]. A fault can be regarded as an inner boundary embedded in a continuous body where a relative displacement between corresponding points is allowed whenever the stress state violates a certain failure criterion. The failure criterion commonly used to describe the fault behavior at the macro-scale is based on the classical Mohr–Coulomb framework [42].

At any point **x** of the fault, the acting strength can be decomposed into two components, σ_n and τ_s, oriented normally and tangentially to the contact surfaces, respectively. The Mohr–Coulomb failure criterion prescribes that the continuity of the displacement across the fault is preserved if:

$$\tau_s \leq \tau_L = c - \sigma_n \tan\varphi, \quad \text{and} \quad \sigma_n < 0 \tag{1}$$

where φ and c are the fault friction angle and cohesion, respectively, and τ_L is the limit shear strength. Conventionally, a negative normal stress means compression. When in equation (1) $\tau_s = \tau_L$ the shear stress can no longer increase and
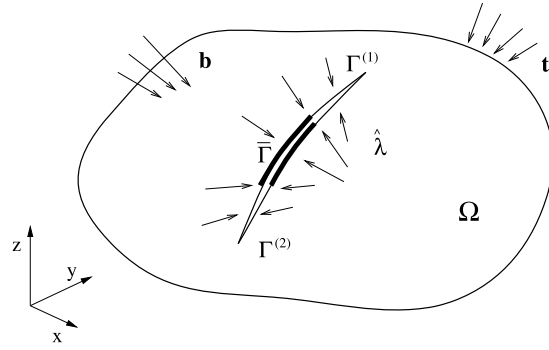
Fig. 1. Conceptual scheme for the fault modeling.

slippage, i.e., a relative surface displacement along the fault plane, can occur. Usually, it is conservatively assumed that faults cannot resist to tensile strengths, so that σ_n cannot be positive. An opening, i.e., a relative displacement in the direction normal to the fault surfaces, can occur if $\sigma_n = 0$. In this case, $\tau_L = 0$ and slippage is allowed as well. The friction coefficient φ can be modeled as a non-linear function of the fault slippage, as proposed for instance in [43–45]. These models are typically based on laboratory experiments of frictional sliding on rock surfaces. In the absence of this information a static friction model, where φ is a constant, is commonly assumed.

The Mohr–Coulomb failure criterion (1) provides the limiting shear strength τ_L for the slippage inception, but gives no indication as to the direction of the limiting shear vector $\boldsymbol{\tau}_L$. To this aim, the "Principle of Maximum Plastic Dissipation" [39,40] can be used. In this problem, such a principle can be formulated as follows. Consider the set $\mathcal{T} \subset \mathbb{R}^3$ of vectors $\boldsymbol{\tau}(\mathbf{x})$ lying in the fault plane and such that $\|\boldsymbol{\tau}(\mathbf{x})\|_2 = \tau_L$. The shear vector $\boldsymbol{\tau}_L \in \mathcal{T}$ acting at the point $\mathbf{x}$, when a relative displacement $\mathbf{u}_r$ between the fault surfaces occurs, is the one that maximizes the work W_f of the friction strength, i.e., the dissipated plastic energy. As W_f reads:

$$W_f(\mathbf{x}) = \boldsymbol{\tau}(\mathbf{x})^T \mathbf{u}_r, \qquad \forall \, \boldsymbol{\tau}(\mathbf{x}) \in \mathcal{T} \tag{2}$$

the vector $\boldsymbol{\tau}_L$ satisfying the principle must have the same direction as $\mathbf{u}_r$, i.e.:

$$\boldsymbol{\tau}_L = \tau_L \frac{\mathbf{u}_r}{\|\mathbf{u}_r\|_2} \tag{3}$$

The use of equation (3) in combination with equation (1) uniquely defines the fault strength at any point $\mathbf{x}$ of the contact surfaces.

2.1. Variational formulation

The problem of finding the displacement $\hat{\mathbf{u}}(\mathbf{x})$ in equilibrium with a given set of external forces can be solved by using the virtual work equation. The enforcement of the contact constraints acts as a restriction of the solution space, that can be addressed with the aid of the Lagrange multipliers [38]. In the case of contact problems [40,41], the Lagrange multipliers $\hat{\boldsymbol{\lambda}}$ physically represent the strengths acting on the discontinuity surfaces and ensuring the continuity of the displacement $\hat{\mathbf{u}}$ across the fault wherever the Mohr–Coulomb criterion (1) is verified. If the condition (1) is not verified, because either $\tau_s = \tau_L$ or $\sigma_n = 0$, the fault strengths are known and can be regarded as external forces, while the contact surfaces are free to develop relative movements. In the context of the present geomechanical application, the contact forces are freely oriented, thus including both the normal and the tangential contribution.

Let us consider a 3D domain Ω bounded by the frontier $\partial\Omega$ and subject to the set of body forces $\mathbf{b}$ and surface tractions $\mathbf{t}$ (Fig. 1). The fault Γ in Ω is identified by a pair of inner surfaces, $\Gamma^{(1)}$ and $\Gamma^{(2)}$, where the strengths $\hat{\boldsymbol{\lambda}}$ are such that the displacement continuity is ensured wherever condition (1) is verified. By distinction, $\overline{\Gamma} \subseteq \Gamma$ denotes the fault portion where condition (1) is not verified and a relative displacement between the contact surfaces can take place. The relative displacement $\mathbf{u}_r$ is conventionally defined as the movement $\hat{\mathbf{u}}^{(2)}$ of $\Gamma^{(2)}$ with respect to $\hat{\mathbf{u}}^{(1)}$ occurring on $\Gamma^{(1)}$:

$$\mathbf{u}_r = \hat{\mathbf{u}}^{(2)} - \hat{\mathbf{u}}^{(1)} \tag{4}$$

If the fault slips, the shear strength on $\overline{\Gamma}$ is $\hat{\lambda}_s(\mathbf{x}) = \boldsymbol{\tau}_L$ of equation (3). If the fault opens, the normal and shear strength on $\overline{\Gamma}$ is $\hat{\lambda}_n(\mathbf{x}) = \hat{\lambda}_s(\mathbf{x}) = 0$. The virtual work equation reads:

$$\delta W_i + \delta W_f - \delta W_e = 0 \tag{5}$$

where δW_i, δW_f and δW_e are the internal, fault and external virtual works, respectively. Following the classical Voigt notation for stress and strain [46], the internal virtual work reads:

$$\delta W_i = \int\limits_\Omega \delta\boldsymbol{\epsilon}^T \hat{\boldsymbol{\sigma}} \, dV \tag{6}$$

where $\boldsymbol{\epsilon} = [\epsilon_x, \epsilon_y, \epsilon_z, \gamma_{xy}, \gamma_{yz}, \gamma_{xz}]^T$ is the strain vector and $\hat{\boldsymbol{\sigma}} = [\hat{\sigma}_x, \hat{\sigma}_y, \hat{\sigma}_z, \hat{\tau}_{xy}, \hat{\tau}_{yz}, \hat{\tau}_{xz}]^T$ is the total stress vector. Recalling Terzaghi's principle for porous media:

$$\hat{\boldsymbol{\sigma}} = \boldsymbol{\sigma} - \alpha p \mathbf{i} \tag{7}$$

with $\boldsymbol{\sigma}$ the effective stress vector, α the Biot coefficient, p the pore fluid pressure and $\mathbf{i} = [1, 1, 1, 0, 0, 0]^T$ the Kronecker delta in vectorial form, equation (6) provides:

$$\delta W_i = \int\limits_\Omega \delta\boldsymbol{\epsilon}^T \boldsymbol{\sigma} \, dV - \int\limits_\Omega \delta\boldsymbol{\epsilon}^T \mathbf{i}\alpha p \, dV \tag{8}$$

The fault virtual work consists of two contributions: (i) the term due to the virtual displacements and strengths along the portion of Γ where the continuity of the solution is prescribed, and (ii) the term due to the fault opening and sliding along the activated part $\overline{\Gamma}$. As in case of opening the normal and shear strengths $\hat{\lambda}_n$ and $\hat{\lambda}_s$ are null, a non-zero contribution to the virtual work is provided only by the shear strength $\hat{\lambda}_s$ during a sliding occurrence:

$$\delta W_f = \int\limits_{\Gamma \backslash \overline{\Gamma}} \delta\mathbf{u}_r^T \hat{\boldsymbol{\lambda}} \, dS + \int\limits_{\Gamma \backslash \overline{\Gamma}} \delta\hat{\boldsymbol{\lambda}}^T \mathbf{u}_r \, dS + \int\limits_{\overline{\Gamma}} \delta\mathbf{u}_r^T \boldsymbol{\tau}_L \, dS \tag{9}$$

Using equations (8) and (9) into (5) and writing explicitly the contribution due to the external body force $\mathbf{b}$ and surface traction $\mathbf{t}$ provides the final mathematical expression for the virtual work theorem:

$$\int\limits_\Omega \delta\boldsymbol{\epsilon}^T \boldsymbol{\sigma} \, dV + \int\limits_{\Gamma \backslash \overline{\Gamma}} \delta\mathbf{u}_r^T \hat{\boldsymbol{\lambda}} \, dS + \int\limits_{\Gamma \backslash \overline{\Gamma}} \delta\hat{\boldsymbol{\lambda}}^T \mathbf{u}_r \, dS + \int\limits_{\overline{\Gamma}} \delta\mathbf{u}_r^T \boldsymbol{\tau}_L \, dS = \int\limits_\Omega \delta\boldsymbol{\epsilon}^T \mathbf{i}\alpha p \, dV + \int\limits_\Omega \delta\hat{\mathbf{u}}^T \mathbf{b} \, dV + \int\limits_{\partial\Omega} \delta\hat{\mathbf{u}}^T \mathbf{t} \, dS \tag{10}$$

In this work we use a one-way coupled approach. Therefore, the pore pressure p is provided by a flow model and its contribution for the equilibrium of the porous matrix is regarded as an external source of strength.

2.2. Numerical model

The variational form (10) is numerically solved by the FE method using a node-to-node geometrical formulation. The displacement $\hat{\mathbf{u}}(\mathbf{x})$ is approximated by the function $\mathbf{u}^h(\mathbf{x}) \in \mathcal{U}^h$, where $\mathcal{U}^h$ is the finite Hilbert function space generated by the piecewise polynomials ℓ_i, $i = 1, \dots, n_\Omega$, with n_Ω the number of FE nodes in Ω:

$$\mathbf{u}^h(\mathbf{x}) = \begin{bmatrix} u_x^h(\mathbf{x}) \\ u_y^h(\mathbf{x}) \\ u_z^h(\mathbf{x}) \end{bmatrix} = \begin{bmatrix} \sum_{i=1}^{n_\Omega} \ell_i(\mathbf{x}) u_{x,i} \\ \sum_{i=1}^{n_\Omega} \ell_i(\mathbf{x}) u_{y,i} \\ \sum_{i=1}^{n_\Omega} \ell_i(\mathbf{x}) u_{z,i} \end{bmatrix} = N_u(\mathbf{x})\mathbf{u} \tag{11}$$

Similarly, the fault strength $\hat{\lambda}(\mathbf{x})$ is approximated by $\lambda^h(\mathbf{x}) \in \mathcal{L}^h$, with $\mathcal{L}^h$ another finite Hilbert function space generated by the set of piecewise polynomials ϕ_j, $j = 1, \dots, n_\Gamma$, n_Γ being the number of FE nodes in $\Gamma^{(1)}$ and $\Gamma^{(2)}$:

$$\boldsymbol{\lambda}^h(\mathbf{x}) = \begin{bmatrix} \lambda_x^h(\mathbf{x}) \\ \lambda_y^h(\mathbf{x}) \\ \lambda_z^h(\mathbf{x}) \end{bmatrix} = \begin{bmatrix} \sum_{j=1}^{n_\Gamma} \phi_j(\mathbf{x}) \lambda_{x,j} \\ \sum_{j=1}^{n_\Gamma} \phi_j(\mathbf{x}) \lambda_{y,j} \\ \sum_{j=1}^{n_\Gamma} \phi_j(\mathbf{x}) \lambda_{z,j} \end{bmatrix} = N_\lambda(\mathbf{x})\boldsymbol{\lambda}_g \tag{12}$$

The fault strengths are more conveniently expressed in a local reference frame. For each element that discretizes the surfaces $\Gamma^{(1)}$ and $\Gamma^{(2)}$ the local reference frame $\xi - \eta - \zeta$ is defined such that the ζ axis identifies the normal direction to the contact surfaces, conventionally oriented from $\Gamma^{(1)}$ to $\Gamma^{(2)}$, and the transversal directions ξ and η are defined so as to constitute an anticlockwise tern with ζ. Introducing the rotation matrix R that transforms the local nodal strengths $\boldsymbol{\lambda}$ into the global vector $\boldsymbol{\lambda}_g$ we have:

$$\boldsymbol{\lambda}^h(\mathbf{x}) = N_\lambda R \boldsymbol{\lambda} \tag{13}$$

Under the hypothesis of small deformations, the approximate strain $\boldsymbol{\epsilon}^h$ is expressed as:

$$\boldsymbol{\epsilon}^h = L\mathbf{u}^h = LN_u\mathbf{u} = B\mathbf{u} \tag{14}$$

where L is the usual first-order differential operator relating the strain to the displacement, and B is the deformation matrix. The approximate effective stress $\boldsymbol{\sigma}^h$ depends on the strain according to the selected constitutive model, that can be written in the classical incremental form:

$$d\boldsymbol{\sigma}^h = D_t \, d\boldsymbol{\epsilon}^h \tag{15}$$

with D_t the tangent constitutive matrix.

In equation (10) the novel contribution is represented by the virtual work due to the fault sliding over $\overline{\Gamma}$. The relative displacement $\mathbf{u}_r^h$ along $\overline{\Gamma}$ in the discrete space $\mathcal{U}^h$ is defined as:

$$\mathbf{u}_r^h = \mathbf{u}^{h,(2)} - \mathbf{u}^{h,(1)} \tag{16}$$

where $\mathbf{u}^{h,(1)}$ and $\mathbf{u}^{h,(2)}$ are the restriction of $\mathbf{u}^h$ over $\overline{\Gamma}^{(1)}$ and $\overline{\Gamma}^{(2)}$, respectively. Using the matrices $S^{(1)}$ and $S^{(2)}$ that map the nodal displacements on the fault surfaces from the global nodal displacement vector $\mathbf{u}$, we obtain:

$$\mathbf{u}_r^h = N_u S^{(2)} \mathbf{u} - N_u S^{(1)} \mathbf{u} = N_u S \mathbf{u} \tag{17}$$

with $S = S^{(2)} - S^{(1)}$. The discrete shear strength $\boldsymbol{\tau}_L^h$ along $\overline{\Gamma}$ depends on τ_L and $\mathbf{u}_r^h$ according to the principle of maximum plastic dissipation (equation (3)). Using the discrete function $\boldsymbol{\lambda}^h$ defined in equation (13), τ_L reads:

$$\tau_L = c - \tan\varphi \mathbf{n}^T N_\lambda R \boldsymbol{\lambda} \tag{18}$$

where $\mathbf{n}$ is the normal vector to $\overline{\Gamma}$, conventionally oriented from $\Gamma^{(1)}$ to $\Gamma^{(2)}$. Introducing equations (17) and (18) into (3), with $\mathbf{u}_r^h$ that replaces $\mathbf{u}_r$, provides the expression of $\boldsymbol{\tau}_L^h$:

$$
\begin{aligned}
\boldsymbol{\tau}_L^h &= \left(c - \tan\varphi \mathbf{n}^T N_\lambda R \boldsymbol{\lambda} \right) \frac{N_u S \mathbf{u}}{\sqrt{\mathbf{u}^T S^T N_u^T N_u S \mathbf{u}}} \\
&= \left(c - \tan\varphi \mathbf{n}^T N_\lambda R \boldsymbol{\lambda} \right) \frac{N_u S \mathbf{u}}{\|\mathbf{u}\|_H}
\end{aligned}
\tag{19}
$$

In equation (19) $\|\mathbf{u}\|_H$ is the H-energy norm of $\mathbf{u}$:

$$\|\mathbf{u}\|_H = \sqrt{\mathbf{u}^T H \mathbf{u}} \tag{20}$$

with $H = S^T N_u^T N_u S$. Notice that H is positive semi-definite because S has not full rank, hence $\|\mathbf{u}\|_H$ is a semi-norm that can be zero even if $\mathbf{u} \neq 0$.

The final numerical model is obtained by introducing all the approximations above in equation (10):

$$
\delta\mathbf{u}^T \int_\Omega B^T \boldsymbol{\sigma}^h dV + \delta\mathbf{u}^T \int_{\Gamma\backslash\overline{\Gamma}} S^T N_u^T N_\lambda R \boldsymbol{\lambda} dS + \delta\boldsymbol{\lambda}^T \int_{\Gamma\backslash\overline{\Gamma}} R^T N_\lambda^T N_u S \mathbf{u} dS +
$$

$$
+ \delta\mathbf{u}^T \int_{\overline{\Gamma}} \left(c - \tan\varphi \mathbf{n}^T N_\lambda R \boldsymbol{\lambda} \right) \frac{H\mathbf{u}}{\|\mathbf{u}\|_H} dS = \delta\mathbf{u}^T \int_\Omega B^T \mathbf{i}\alpha p dV + \delta\mathbf{u}^T \int_\Omega N_u^T \mathbf{b} dV + \delta\mathbf{u}^T \int_{\partial\Omega} N_u^T \mathbf{t} dS \tag{21}
$$

The equation (21) must hold true for any virtual displacement $\delta\mathbf{u}$ and virtual strength $\delta\boldsymbol{\lambda}$. Setting:

$$C = \int_{\Gamma\backslash\overline{\Gamma}} S^T N_u^T N_\lambda R dS \tag{22}$$

$$\mathbf{f} = \int_\Omega B^T \mathbf{i}\alpha p dV + \int_\Omega N_u^T \mathbf{b} dV + \int_{\partial\Omega} N_u^T \mathbf{t} dS \tag{23}$$

equation (21) can be recast as a non-linear system in the unknowns $\mathbf{u}$ and $\boldsymbol{\lambda}$:

$$
\begin{cases}
\int_\Omega B^T \boldsymbol{\sigma}^h dV + C\boldsymbol{\lambda} + \int_{\overline{\Gamma}} \left(c - \tan\varphi \mathbf{n}^T N_\lambda R \boldsymbol{\lambda} \right) \frac{H\mathbf{u}}{\|\mathbf{u}\|_H} dS - \mathbf{f} = 0 \\
C^T \mathbf{u} = 0
\end{cases}
\tag{24}
$$

i.e.:

$$
\begin{cases}
\mathbf{F}_1(\mathbf{u}, \boldsymbol{\lambda}) = 0 \\
\mathbf{F}_2(\mathbf{u}, \boldsymbol{\lambda}) = 0
\end{cases}
\tag{25}
$$

The numerical solution to (25) is obtained with a classical Newton–Raphson scheme. The Jacobian matrix $J(\mathbf{u}, \boldsymbol{\lambda})$ can be written in a 2×2 block form:

$$
J = \begin{bmatrix} J_{11} & J_{12} \\ J_{21} & J_{22} \end{bmatrix}
\tag{26}
$$

where:

$$J_{11} = \frac{\partial \mathbf{F}_1}{\partial \mathbf{u}} = \int_{\Omega} B^T D_t B dV + \int_{\overline{\Gamma}} \left(c - \tan \varphi \mathbf{n}^T N_\lambda R \boldsymbol{\lambda} \right) \frac{\|\mathbf{u}\|_H^2 H - (H\mathbf{u})(H\mathbf{u})^T}{\|\mathbf{u}\|_H^3} dS = K(\mathbf{u}) + E(\mathbf{u}, \boldsymbol{\lambda}) \tag{27}$$

$$J_{12} = \frac{\partial \mathbf{F}_1}{\partial \boldsymbol{\lambda}} = C - \int_{\overline{\Gamma}} \tan \varphi \frac{H\mathbf{u}}{\|\mathbf{u}\|_H} \mathbf{n}^T N_\lambda R dS = C - F(\mathbf{u}) \tag{28}$$

$$J_{21} = \frac{\partial \mathbf{F}_2}{\partial \mathbf{u}} = C^T \tag{29}$$

$$J_{22} = \frac{\partial \mathbf{F}_2}{\partial \boldsymbol{\lambda}} = 0 \tag{30}$$

Details on the form of the local contributions to C, E and F are provided in Appendix A. The solution $(\mathbf{u}, \boldsymbol{\lambda})$ is therefore obtained starting from an initial guess $(\mathbf{u}^{(0)}, \boldsymbol{\lambda}^{(0)})$ with the following iterative scheme:

$$\begin{bmatrix} \mathbf{u}^{(k+1)} \\ \boldsymbol{\lambda}^{(k+1)} \end{bmatrix} = \begin{bmatrix} \mathbf{u}^{(k)} \\ \boldsymbol{\lambda}^{(k)} \end{bmatrix} + \begin{bmatrix} \Delta \mathbf{u} \\ \Delta \boldsymbol{\lambda} \end{bmatrix} \tag{31}$$

The corrections $\Delta \mathbf{u}$ and $\Delta \boldsymbol{\lambda}$ are computed by solving a linear system with the Jacobian matrix $J^{(k)} = J(\mathbf{u}^{(k)}, \boldsymbol{\lambda}^{(k)})$:

$$\begin{bmatrix} K(\mathbf{u}^{(k)}) + E(\mathbf{u}^{(k)}, \boldsymbol{\lambda}^{(k)}) & C - F(\mathbf{u}^{(k)}) \\ C^T & 0 \end{bmatrix} \begin{bmatrix} \Delta \mathbf{u} \\ \Delta \boldsymbol{\lambda} \end{bmatrix} = - \begin{bmatrix} \mathbf{F}_1(\mathbf{u}^{(k)}, \boldsymbol{\lambda}^{(k)}) \\ \mathbf{F}_2(\mathbf{u}^{(k)}, \boldsymbol{\lambda}^{(k)}) \end{bmatrix} \tag{32}$$

The Jacobian $J^{(k)}$ is a non-symmetric generalized saddle-point matrix [47]. It can be shown (see Appendix A) that the $(1, 1)$ block $K + E$ is still symmetric positive definite if K is so. Anyway, the linearized step (32) has to be solved by a non-symmetric solver.

The convergence of the Newton–Raphson procedure (31) is achieved when some vector norm falls below a prescribed tolerance. Possible choices are as follows:

1. the norm of the displacement increment, i.e., $r_u = \|\Delta \mathbf{u}\|$;
2. the norm of the unbalanced forces, i.e., $r_f = \|\mathbf{F}_1(\mathbf{u}^{(k)}, \boldsymbol{\lambda}^{(k)})\|$;
3. the deformation energy, that is computed as $r_e = |\Delta \mathbf{u}^T \mathbf{F}_1(\mathbf{u}^{(k)}, \boldsymbol{\lambda}^{(k)}) + \Delta \boldsymbol{\lambda}^T \mathbf{F}_2 (\mathbf{u}^{(k)}, \boldsymbol{\lambda}^{(k)})|$.

The norms above are usually normalized by their initial value. Different values for the exit tolerance have to be set in order to guarantee the same solution accuracy when using different vector norms. The norm of the unbalanced forces r_f is the most demanding one, while the energy norm r_e is the weakest, so that an exit tolerance set to 10^{-10} for r_f may correspond to 10^{-20} or less for r_e.

2.3. Implementation details

The main non-linearity of the proposed model stems from the activation of a fault portion. A major difficulty with this formulation is that $\overline{\Gamma}$ is itself unknown and has to be computed during the non-linear iterations. In the present approach, three operating modes are possible for a pair of corresponding nodes on $\Gamma^{(1)}$ and $\Gamma^{(2)}$.

1. Full opening: the nodes are not in contact and a free relative displacement is allowed. The Lagrange multipliers are known and equal to zero.
2. Full closure: the fault is compressed and the Mohr–Coulomb criterion (1) is satisfied. The Lagrange multipliers are unknown and such that no relative movement is allowed for between two corresponding nodes.
3. Slipping: the fault is compressed, but the limit shear strength is not able to prevent sliding. The Lagrange multiplier λ_ζ acting on the normal direction is unknown, while the components lying on the contact surface are computed using equation (3).

The algorithm summarizing the sequence of steps that control the fault activation is provided in Table 1. Lines in italic are comments. For each node pair j lying on Γ, the relative displacement $\mathbf{u}_{r,j}$ of $\Gamma^{(2)}$ with respect to $\Gamma^{(1)}$ is computed. If either the normal component of $\mathbf{u}_{r,j}$ or the normal stress $\lambda_{\zeta,j}$ obtained from the last linearized step is positive, then the contact surfaces open at the node pair j and the Lagrange multipliers are zero. At the following solution of system (32), the nodes of the pair j on $\Gamma^{(1)}$ and $\Gamma^{(2)}$ can move freely. Because of rounding errors the check on the opening condition is relaxed by using the tolerances ε_u and ε_n on the normal displacement and stress, respectively. If the opening check is not satisfied, the current tangential stress τ and the limiting value τ_L are computed. If τ does not exceed the limiting value τ_L, the node pair j is closed and the related contributions to C and C^T are computed. The Lagrange multipliers at j

Table 1
Algorithm for the control of the fault activation.

1.	FOR $j = 1, \ldots, n_\Gamma$
2.	Compute the relative displacement $\mathbf{u}_{r,j}$
3.	IF $(\mathbf{n}_j^T \mathbf{u}_{r,j} > \varepsilon_u) \vee (\lambda_{\zeta,j} \geq \varepsilon_n)$ THEN
4.	*Full opening mode: Lagrange multipliers are zero*
5.	$\lambda_{\zeta,j} = \lambda_{\xi,j} = \lambda_{\eta,j} = 0$
6.	ELSE
7.	*Full closure or Slipping mode: check the tangential stress*
8.	$\tau = \sqrt{\lambda_{\xi,j}^2 + \lambda_{\eta,j}^2}$
9.	$\tau_L = c - \lambda_{\zeta,j} \tan \varphi$
10.	IF $(\tau < \tau_L + \varepsilon_t)$ THEN
12.	*Full closure mode: Lagrange multipliers are unknown*
13.	Compute the contribution of node j to C and C^T
14.	ELSE
15.	*Slipping mode: only the Lagrange multiplier $\lambda_{\zeta,j}$ is unknown*
16.	Compute the contribution of node j to C and C^T related to $\lambda_{\zeta,j}$
17.	IF $(\|\mathbf{u}_{r,j}\|_2 > \varepsilon_u)$ THEN
18.	Compute the contribution to E and $-F$
19.	END IF
20.	END IF
21.	END IF
22.	END FOR

are unknown and so as to ensure the displacement continuity through $\Gamma^{(1)}$ and $\Gamma^{(2)}$. Otherwise, if τ exceeds the limiting value τ_L the nodes of the pair j can slide. The stress components on the surface plane $\lambda_{\xi,j}$ and $\lambda_{\eta,j}$ are not considered as unknowns in the solution of system (32) and are computed according to equation (3). By distinction, $\lambda_{\zeta,j}$ is still unknown and its contribution to C and C^T must be accounted for. Again, because of the rounding errors it is advisable to relax the check on τ_L by introducing another tolerance ε_t. In the slipping mode, the local contributions to E and $-F$ have to be computed as well. As shown in equations (27) and (28), the matrices E and $-F$ depend on $\|\mathbf{u}\|_H$ that locally coincides with $\|\mathbf{u}_{r,j}\|_2$ (see Appendix A). If the current shear stress exceeds the limiting value τ_L but the sliding is close to zero, the coefficients of E and $-F$ can numerically become unstable. Actually, if the limiting shear stress is exceeded with no sliding there's no friction work on $\overline{\Gamma}$ and the contributions E and $-F$ should be zero. This is why these terms are computed only if $\|\mathbf{u}_{r,j}\|_2$ is "large enough", i.e., is numerically larger than the tolerance ε_u.

3. Numerical results

The numerical model for the mechanics of faults and fractures has been implemented and tested in some examples. The current implementation uses linear piecewise polynomials for $\mathbf{u}^h$ and constant piecewise polynomials for $\boldsymbol{\lambda}^h$ (Appendix A). With this choice the discontinuity strengths are consistent with the stress computed in the finite elements that discretize the continuous porous body. Quite obviously, other choices are possible, but more stable results are typically obtained using for the Lagrange multipliers a lower-order approximation than for the displacements.

Three test cases are investigated herein.

- Test Case A: single crack under compression in plane stress conditions. As the analytical solution is available [48], this test case is used to validate the proposed formulation.
- Test Case B: two adjacent blocks under compression and shear. This example is used to investigate the numerical convergence of the non-linear algorithm, along with its robustness and stability.
- Test Case C: ground fracture due to groundwater withdrawal in arid regions. This is a realistic engineering problem, already presented in [49], used to validate the proposed model in a large-size application.

3.1. Test Case A: single crack under compression in plane stress conditions

A single crack in an unbounded domain with plane stress conditions and subject to a compressive external remote stress σ is studied. The material is linear elastic with Young modulus $E = 70$ GPa and Poisson ratio $\nu = 0.2$. The crack length and inclination angle are $2b = 10$ m and $\alpha = 20°$, respectively (Fig. 2). Assuming $\sigma = 200$ MPa with zero cohesion and friction angle $\varphi = 30°$, the crack surfaces slide with the following analytical results for the normal stress σ_n and slip Δu_t [48]:
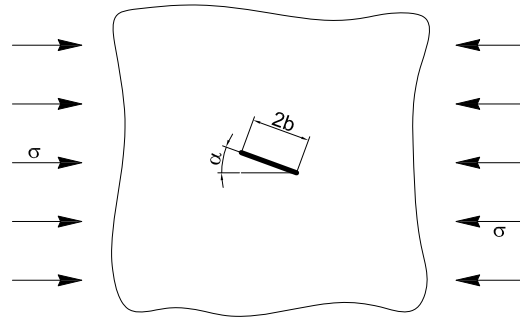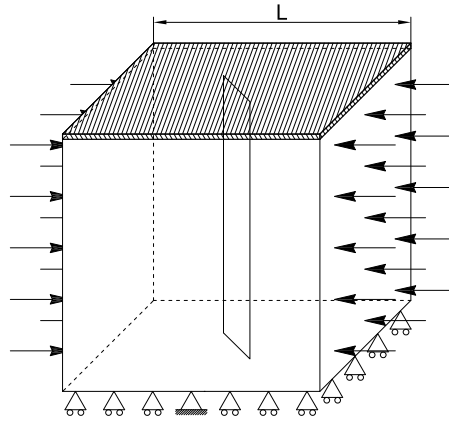
Fig. 2. Test Case A.

Fig. 3. 3D model for Test Case A.

$$\sigma_n = -\sigma \sin^2 \alpha \tag{33}$$

$$\Delta u_t = \frac{4\left(1 - \nu^2\right) \sigma \sin\alpha \left(\cos\alpha - \sin\alpha \tan\varphi\right)}{E} \sqrt{b^2 - (\eta - b)^2} \tag{34}$$

where $0 \le \eta \le 2b$ is the linear length coordinate along the crack.

We want to reproduce the 2D plane stress condition of Test Case A with our 3D model. To this aim, a cubic volume with side $L = 500$ m, i.e., 50 times the crack size, is considered, with the boundary conditions shown in Fig. 3. The plane stress condition is obtained on the upper face (hatched in Fig. 3). The FE grid consists of 1,933,830 elements and 347,183 nodes, while the crack is discretized by 2,895 nodes. Fig. 4 provides a comparison between the numerical and analytical solutions along the crack. The results show quite a good agreement, especially on consideration of the approximate representation of the plane stress state condition with our full 3D model. The numerical outcome differs from the analytical solution (33) and (34) by about 2% and less than 1% in terms of σ_n and Δu_t, respectively. Also notice that the larger differences for σ_n at the crack ends are due to the grid size.

3.2. Test Case B: two adjacent blocks under compression and shear

The problem is shown in Fig. 5. A prismatic elastic body is divided in two blocks by a vertical crack. The prism has a rectangular basis 5×10 m wide and is 15-m high. Boundary conditions and loads are prescribed as shown in Fig. 5. The FE grid consists of 36,000 elements and 7,749 nodes, of which 588 are located on the crack. The linear elastic material is characterized by $E = 2$ GPa and $\nu = 0.25$. An initial compressive stress state $\sigma_0 = \sigma_n = 1$ kPa along the x-direction is assumed. The crack has zero cohesion and friction angle $\varphi = 30°$.

The normal and shear loads, N and T, respectively, are varied during the simulation as shown in Fig. 6. At first, the prism, hence the crack, is compressed along the x-direction by an increasing load up to $N = 750$ kN, corresponding to a distributed pressure equal to 5 kPa. Then, the shear force T begins to act, up to $T = 450$ kN, i.e., a uniform vertical pressure on the upper face of the rightmost block equal to 18 kPa is applied. In the second part of the simulation, first N and then T are removed. This way the crack is expected to start slipping as T is increased, with the sliding portion later increasing more rapidly as N decreases. Finally, the reduction of T produces a rebound of the rightmost block. As the initial compressive state σ_0 is still acting, for small values of T the induced shear stress turns to be smaller than the limiting value τ_L and the crack closes again. As a consequence, although at the end of the simulation the loads vanish, the body does not return to the initial configuration.
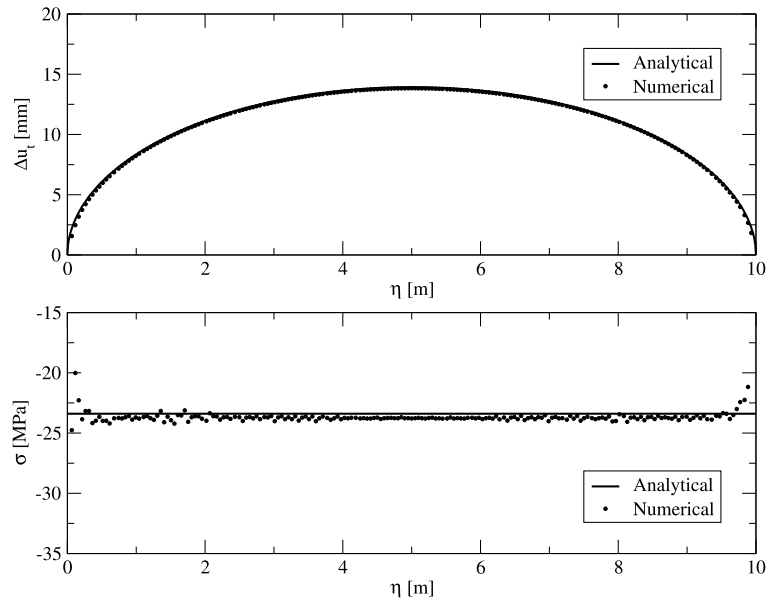
Fig. 4. Test Case A: numerical and analytical solutions along the crack.
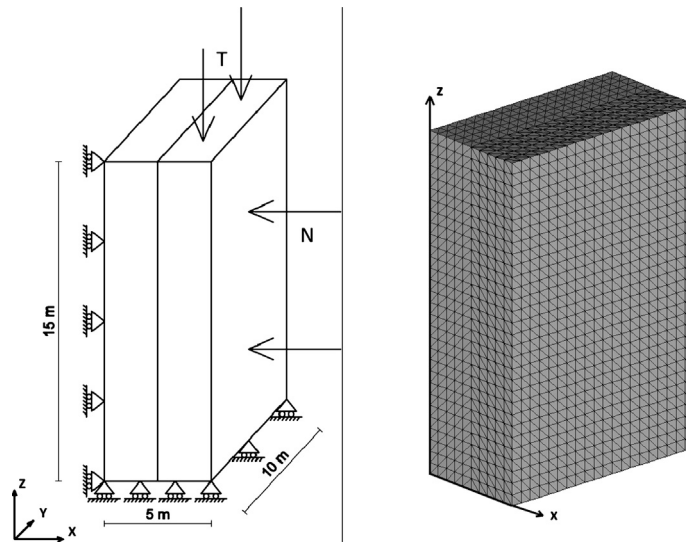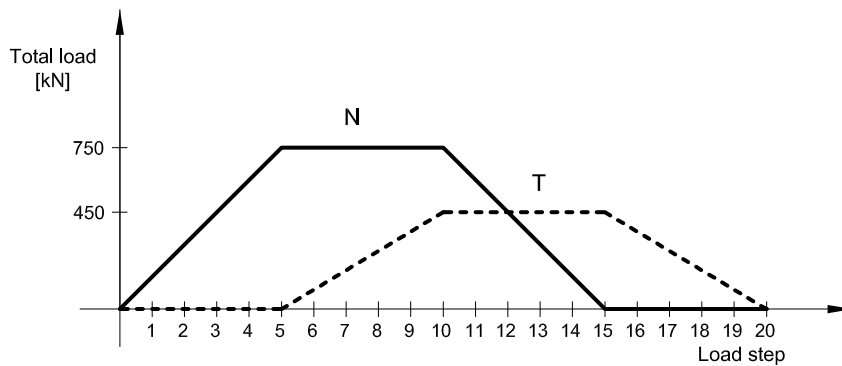

Fig. 5. Test Case B.
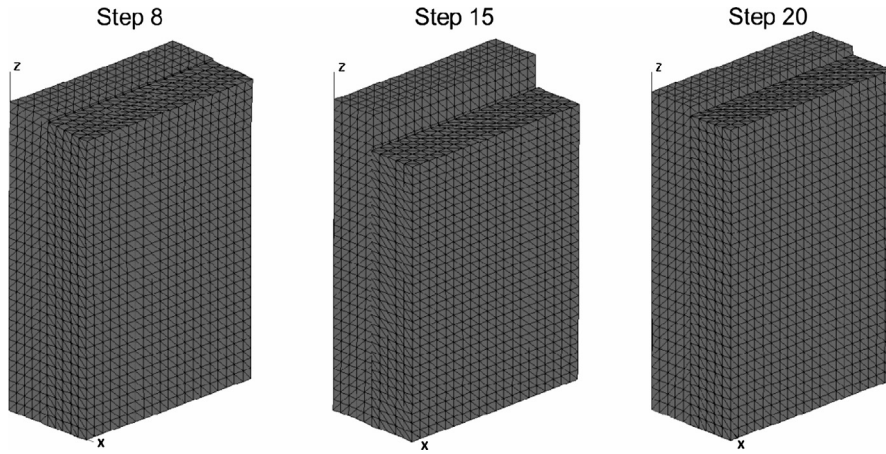

Fig. 6. Test Case B: load history.

Fig. 7. Test Case B: deformed configuration for the load steps no. 8, 15 and 20. The displacement exaggeration factor is 15.
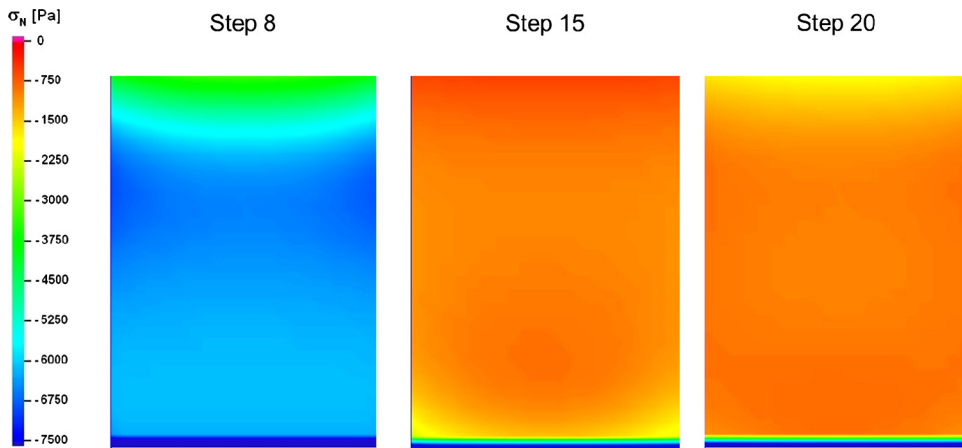

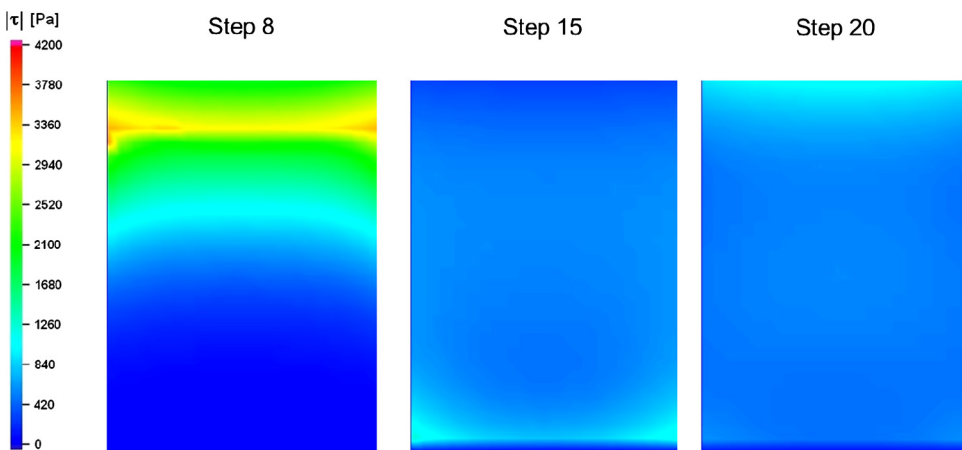**Fig. 8.** Test Case B: normal stress on the crack surface for the load steps no. 8, 15 and 20.

Fig. 9. Test Case B: shear stress on the crack surface for the load steps no. 8, 15 and 20.

The main numerical results are provided in Fig. 7 through Fig. 11. Fig. 7 shows the deformed configuration of the elastic body at some steps of interest, namely the load steps no. 8, 15 and 20, while Figs. 8 and 9 give the normal and shear stress, σ_n and τ_s, respectively, at the same instants. Figs. 10 and 11 provide the behavior of σ_n, τ_s and the relative slip Δu_z in vertical direction along the crack central axis and during the simulation at some points of interest at different elevation z.
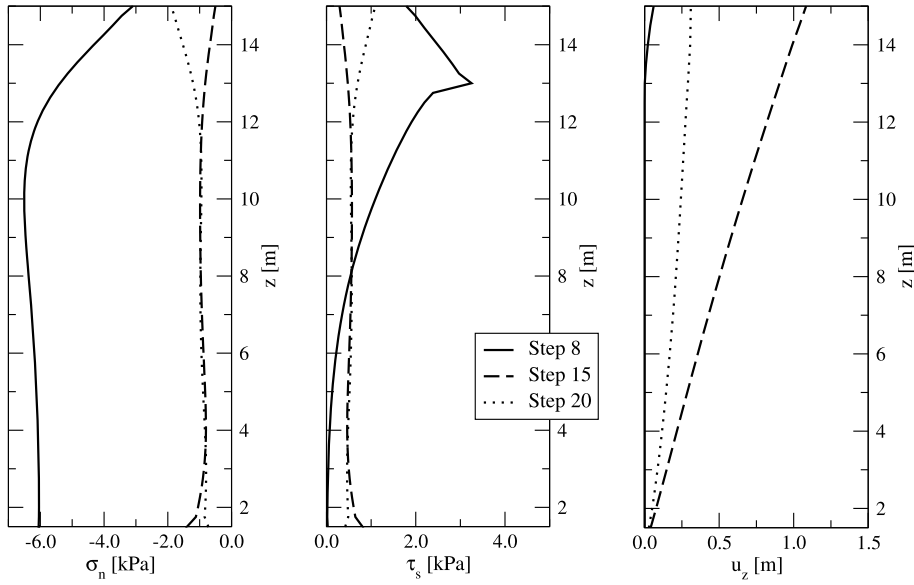
Fig. 10. Test Case B: σ_n, τ_s and Δu_z along the crack central axis for the load steps no. 8, 15, and 20.

Fig. 11. Test Case B: σ_n, τ_s and Δu_z vs load step at different elevation z.
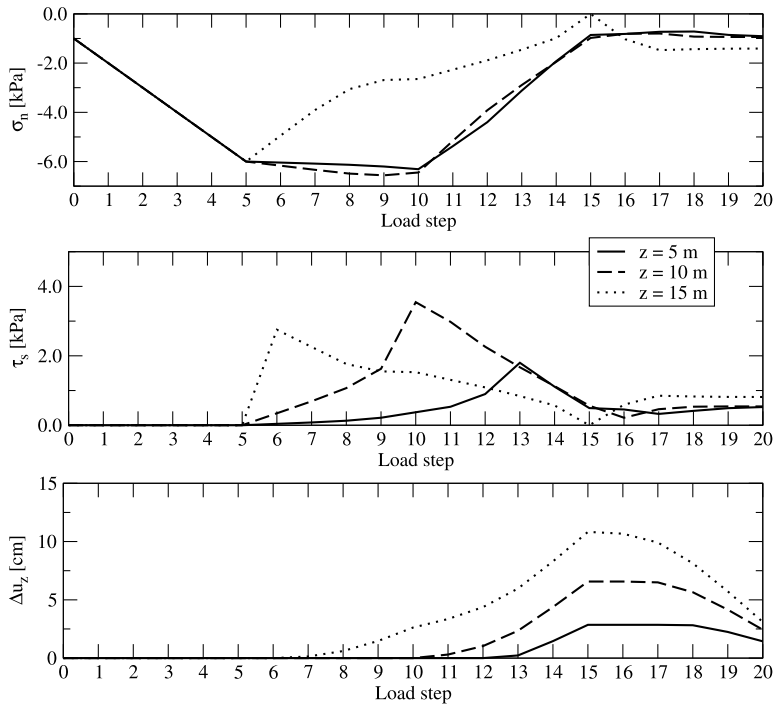
At the step 8, the crack starts sliding in the upper part (see Fig. 10). Figs. 8 and 10 show also a σ_n reduction in this region, which is induced by the T increase. This yields a decrease of the limiting stress τ_L, hence the inception of the sliding condition. At the step 15, the crack is fully sliding. The τ_s reduction is due to the absence of N that reduces σ_n, hence τ_L. In this situation the rightmost volume of the elastic body is almost independent of the leftmost part. At the end of the simulation there are no external loads. The body does not return to the original configuration because of the model non-linearity, i.e., the energy dissipation generated by the fault friction.

Fig. 12 shows four representative convergence profiles of the non-linear algorithm. The selected exit criterion is based on the relative 2-norm of the unbalanced forces, i.e.:
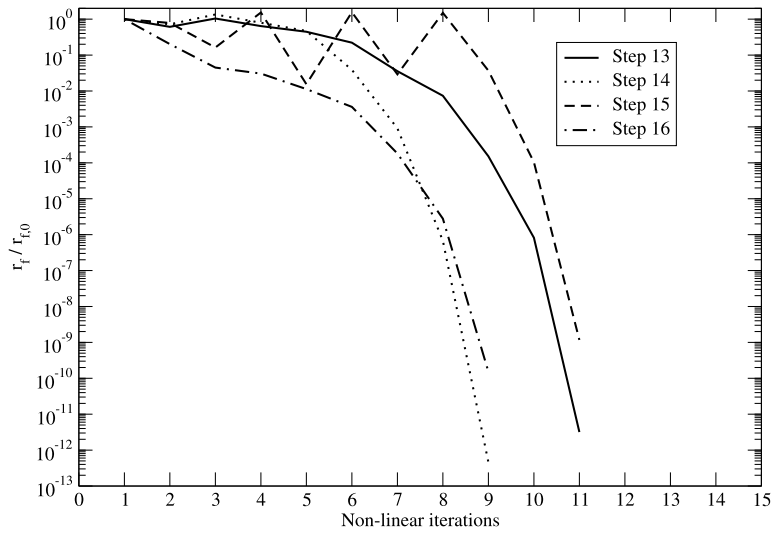
Fig. 12. Test Case B: convergence profile of the non-linear algorithm.
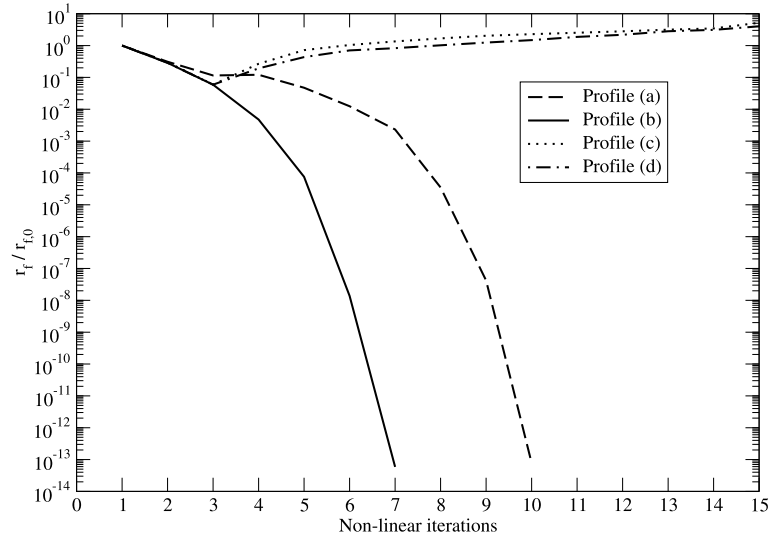

Fig. 13. Test Case B: convergence profile of the non-linear algorithm at step no. 8 (a), halving the load step size (b), and neglecting the numerical contribution of the integral over $\overline{\Gamma}$ in equation (24) for the full (c) and half-size load step (d).

$$\frac{r_f}{r_{f,0}} = \frac{\left\| \mathbf{F}_1(\mathbf{u}^{(k)}, \boldsymbol{\lambda}^{(k)}) \right\|_2}{\left\| \mathbf{F}_1(\mathbf{u}^{(0)}, \boldsymbol{\lambda}^{(0)}) \right\|_2} \tag{35}$$

From the numerical point of view, the steps from 13 to 16 are the most challenging ones because the crack is fully sliding. Nevertheless, the non-linear algorithm exhibits at any step a quadratic convergence.

The novelty of the proposed formulation for the fault simulation relies on the contribution arising from the principle of maximum plastic dissipation, i.e., the integral over $\overline{\Gamma}$ in equation (24) and the related matrices E and $-F$ in the computation of the Jacobian. The numerical importance of such a contribution is emphasized in Fig. 13, where the convergence profiles of the non-linear algorithm at the inception of sliding (step no. 8) are shown for two different sizes of the load step. When a portion of the crack starts sliding, $\overline{\Gamma} \neq \emptyset$ and neglecting the corresponding integral yields a stagnation of the unbalanced forces, possibly far from the equilibrated configuration, independently of the load step size.

3.3. Test Case C: ground fracture due to groundwater withdrawal

The numerical model is tested in a realistic test case simulating the possible generation and evolution of a ground fracture in a 3D geological setting. The case where a rigid basement outcrops and abruptly bounds an alluvial sequence
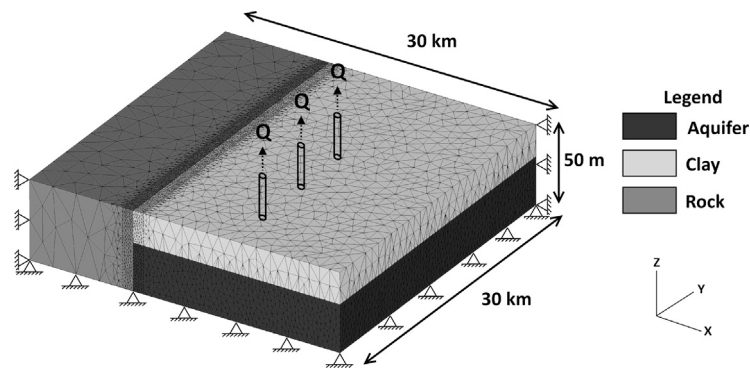
Fig. 14. Test Case C.

Table 2
Test Case C: Young modulus, E, Poisson ratio, ν, and permeability K of the different materials.

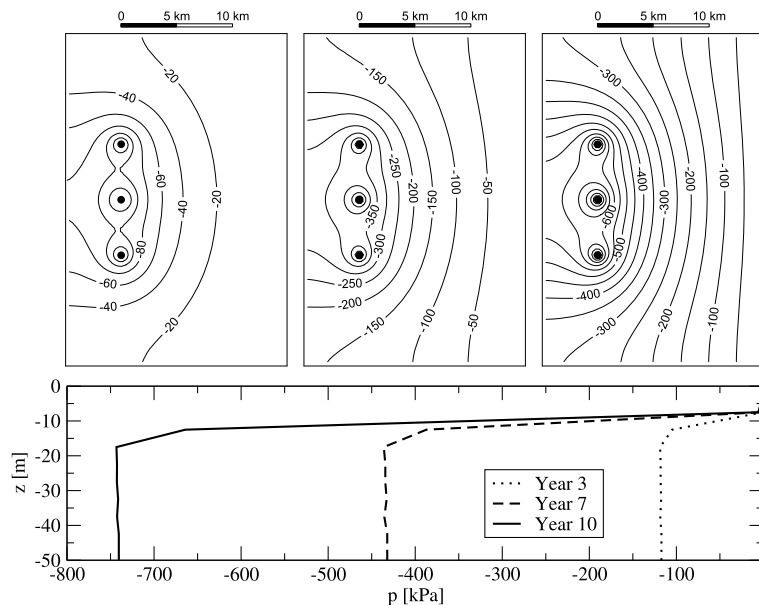| Material	E [MPa]	ν	K [m/s]
Aquifer	15	0.25	10^{-4}
Clay	15	0.25	10^{-10}
Rock	4900	0.25	0

Fig. 15. Test Case C: pressure maps in the aquifer after 3, 7 and 10 years of pumping (above) and along a vertical profile at the central well location (below). Pressure is in kPa.

is investigated. For example, such a situation often occurs in the urban areas located in the lacustrine or fluvio-lacustrine depressions of the central sector of the Mexican volcanic belt, such as Morelia, Celaya, and Queretaro [23].

The problem domain is sketched in Fig. 14. A 30-m thick aquifer is overlain by a 20-m thick clay unit and bounded on a side by an outcropping rock formation that intercepts the sedimentary sequence vertically. The hydro-geomechanical properties of the different materials are summarized in Table 2. For the sake of simplicity, a linear elastic constitutive behavior is assumed. The aquifer is produced for a 10-year period by three wells located at a 5-km distance from the interface between the rock and the alluvial formation (Fig. 14). The pore pressure variation induced in the sandy and clay units (Fig. 15) is used as an external source of strength for the geomechanical model.

The interface between the rock and alluvial formation is modeled as a vertical fault with zero cohesion and friction angle $\varphi = 30°$. The lithostatic load provides the initial stress condition. The overall FE mesh consists of 297,971 elements with 57,050 nodes, of which 4,009 are located on the fault.

The groundwater withdrawal causes both a vertical and lateral contraction of the aquifer, and partially of the overlying clay layer. By distinction, the rock formation is rigid and impervious, hence a fracture can develop at the interface with
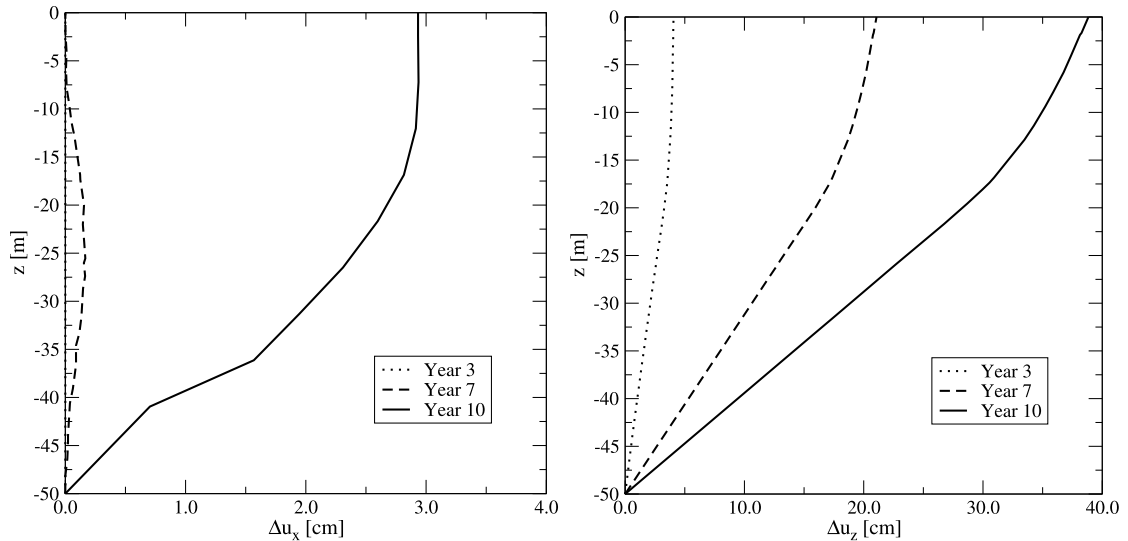
Fig. 16. Test Case C: opening (left) and sliding (right) along the central axis of the fracture.
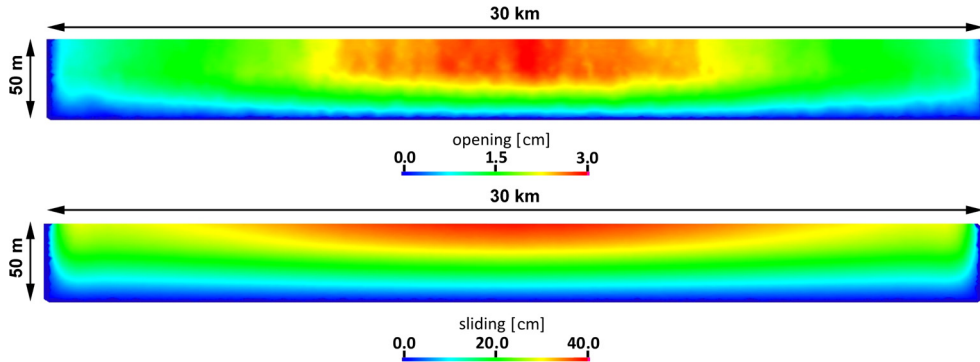

Fig. 17. Test Case C: opening (above) and sliding (below) on the fissure at the end of the simulation.

the alluvial deposits. According to the pressure evolution in time, the fracture starts to slide vertically after 3 years from the inception of pumping. At year 7, the lateral contraction of the aquifer causes an opening that enlarges to the whole contact surface at the end of simulation. Figs. 16 and 17 show that the opening Δu_x and the vertical sliding Δu_z is about 3 and 40 cm on the ground surface, respectively, and that the numerical solution appears to be quite smooth on the contact surface. The generation of the ground fracture has also a significant impact on the land motion. Fig. 18 provides the land subsidence, i.e., the vertical movement of the ground surface, along the x direction, showing that the fissure slip has the same order as the maximum settlement.

Test Case C has been already presented and discussed in [49], where a penalty approach with the explicit algorithms developed in [3] was used. The formulation developed in this work provides a much more stable solution along the fissure, avoiding the numerical oscillations that may typically occur using a penalty approach. For the sake of the comparison, Fig. 19 provides the distribution on the fracture plane of the sliding elements at year 5 obtained with the penalty approach. At this year the fissure is actually completely sliding. The mean slippage of the fracture, computed as the integral average of the relative vertical movements of the nodes at the interface between the rock and the alluvial sediments, is 4.0 cm and 3.8 cm with the penalty and the Lagrangian formulation, respectively, i.e., on the average the two approaches give approximately the same result. However, locally the outcome of the two models can be quite different.

4. Conclusions

A novel formulation based on the use of Lagrange multipliers is developed for the stable and robust numerical modeling of fault mechanics. A fault or fracture is simulated as a pair of inner surfaces included in a 3D geological formation where Lagrange multipliers are used to prescribe the contact constraints. The activation of a fault is controlled by the classical Mohr–Coulomb failure criterion. The standard variational formulation of the contact problem with Lagrange multipliers is modified to take into account the energy dissipated by the frictional work along the activated fault portion. This term is
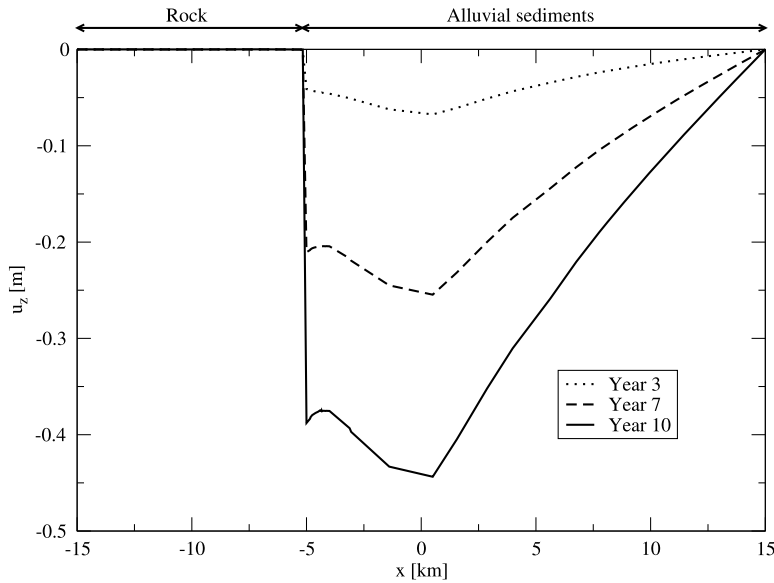
Fig. 18. Test Case C: land subsidence along the *x*-direction on the symmetry axis of the domain.
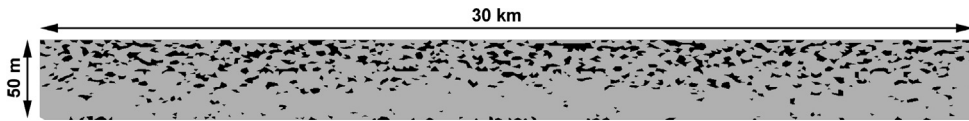

Fig. 19. Test Case C: distribution of sliding (light gray) and non-sliding (dark gray) elements on the fissure at year 5 obtained with a penalty approach [3,49].

computed by making use of the principle of maximum plastic dissipation, whose application defines the direction of the limiting shear stress vector.

The numerical model is developed in the framework of the FE method and gives rise to a non-linear system of algebraic equations. The non-linear system is solved by a Newton–Raphson method where the Jacobian matrix is non-symmetric and has a generalized saddle-point structure. The proposed formulation is validated and investigated in some test cases, using piecewise linear and element-wise constant approximations for displacements and contact strengths, respectively. The following results are worth summarizing:

- the novel formulation has been successfully validated against analytical solutions;
- the non-linear algorithm exhibits a quadratic convergence even in numerically challenging configurations, providing stable and smooth solutions;
- the numerical contribution arising from the application of the principle of maximum plastic dissipation to compute the frictional work on the activated fault portion is decisive to ensure the convergence of the non-linear algorithm;
- by distinction with the classical penalty approach, the numerical solution appears to be much more regular, avoiding local stress oscillations.

Acknowledgements

Appendix A. Local stiffness matrices

A classical FE discretization is used with piecewise linear and constant basis functions for displacements and Lagrange multipliers, respectively. Therefore, the 3D volume Ω and the fault contact surfaces $\Gamma^{(1)}$ and $\Gamma^{(2)}$ are discretized by tetrahedral and triangular elements. For the sake of brevity, we denote as Interface Element (IE) a pair of opposite triangular elements located on the contact surfaces (Fig. A.20). The global contributions C, E and F are computed in the classical FE framework by assembling the local contributions $C^{(e)}$, $E^{(e)}$ and $F^{(e)}$ over each IE.
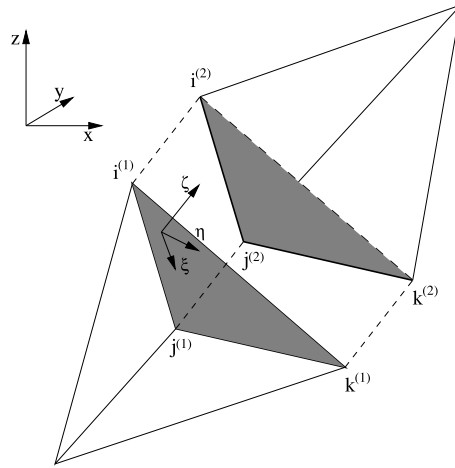
Fig. A.20. Interface element.

The local unknowns defined at the elemental level are the relative displacement $\mathbf{u}_r^{(e)}$ and the contact strength $\boldsymbol{\lambda}^{(e)}$. Recalling the global definitions (16)–(17) and with reference to the element in Fig. A.20, $\mathbf{u}_r^{(e)}$ reads:

$$\mathbf{u}_r^{(e)} = \begin{bmatrix} \mathbf{u}_{r,i} \\ \mathbf{u}_{r,j} \\ \mathbf{u}_{r,k} \end{bmatrix} = \begin{bmatrix} -I_3 & I_3 & 0 & 0 & 0 & 0 \\ 0 & 0 & -I_3 & I_3 & 0 & 0 \\ 0 & 0 & 0 & 0 & -I_3 & I_3 \end{bmatrix} \begin{bmatrix} \mathbf{u}_{i^{(1)}} \\ \mathbf{u}_{i^{(2)}} \\ \mathbf{u}_{j^{(1)}} \\ \mathbf{u}_{j^{(2)}} \\ \mathbf{u}_{k^{(1)}} \\ \mathbf{u}_{k^{(2)}} \end{bmatrix} = S^{(e)} \mathbf{u}^{(e)} \tag{A.1}$$

where $\mathbf{u}_{r,m}$ is the vector of the relative displacements along x, y and z between the opposite nodes $m^{(1)}$ and $m^{(2)}$, and I_n denotes the rank-n identity matrix. The matrix $N_u^{(e)}(\mathbf{x})$ of the local basis functions such that $\mathbf{u}_r^{h,(e)} = N_u^{(e)}(\mathbf{x})\mathbf{u}_r^{(e)}$ is:

$$N_u^{(e)}(\mathbf{x}) = \begin{bmatrix} \psi_i^{(e)}(\mathbf{x}) I_3 & \psi_j^{(e)}(\mathbf{x}) I_3 & \psi_k^{(e)}(\mathbf{x}) I_3 \end{bmatrix} \tag{A.2}$$

The function $\psi_m^{(e)}(\mathbf{x})$ is the restriction on the IE e of the basis functions $\ell_{m^{(1)}}(\mathbf{x})$ and $\ell_{m^{(2)}}(\mathbf{x})$ introduced in equation (11). Similarly, recalling the global definition (13) and with reference to Fig. A.20, $\boldsymbol{\lambda}^{(e)}$ reads:

$$\boldsymbol{\lambda}^{(e)} = \begin{bmatrix} \boldsymbol{\lambda}_i \\ \boldsymbol{\lambda}_j \\ \boldsymbol{\lambda}_k \end{bmatrix} \tag{A.3}$$

where $\boldsymbol{\lambda}_m$ is the vector of the nodal strengths along the local ζ, ξ and η directions acting between the nodes $m^{(1)}$ and $m^{(2)}$. Using the rotation matrix $R^{(e)}$, the matrix $N_\lambda^{(e)}(\mathbf{x})$ of the local basis functions such that $\boldsymbol{\lambda}^{h,(e)} = N_\lambda^{(e)}(\mathbf{x})R^{(e)}\boldsymbol{\lambda}^{(e)}$ is:

$$N_\lambda^{(e)}(\mathbf{x}) = \begin{bmatrix} \phi_i^{(e)}(\mathbf{x}) I_3 & \phi_j^{(e)}(\mathbf{x}) I_3 & \phi_k^{(e)}(\mathbf{x}) I_3 \end{bmatrix} \tag{A.4}$$

with $\phi_m^{(e)}(\mathbf{x})$ the restriction on the IE e of the basis functions $\phi_{m^{(1)}}(\mathbf{x})$ and $\phi_{m^{(2)}}(\mathbf{x})$ of equation (12). In particular, $\phi_m(\mathbf{x})$ is the piecewise constant function defined as follows:
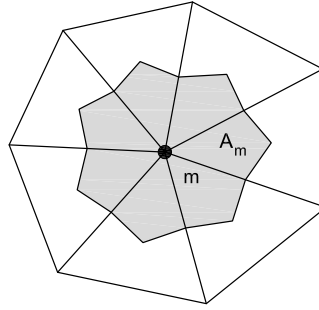
$$\phi_m(\mathbf{x}) = \begin{cases} 1 & \text{if } \mathbf{x} \in A_m \\ 0 & \text{otherwise} \end{cases} \tag{A.5}$$

In equation (A.5) A_m is the area associated to the node m (Fig. A.21), i.e.:

$$A_m = \sum_e \frac{A^{(e)}}{3} \tag{A.6}$$

where $A^{(e)}$ is the area of the triangle e and the sum is performed over all IEs sharing the node m.

By using equations (A.1), (A.2) and (A.4), and recalling the global definition (22), the 18×9 local matrix $C^{(e)}$ can be easily obtained as:

Fig. A.21. Area associated to node m.

$$C^{(e)} = \int_{A^{(e)}} S^{(e),T} N_u^{(e),T} N_\lambda^{(e)} R^{(e)} dS = S^{(e),T} \overline{H}^{(e)} R^{(e)} \tag{A.7}$$

where:

$$\overline{H}^{(e)} = \int_{A^{(e)}} N_u^{(e),T} N_\lambda^{(e)} dS = \frac{A^{(e)}}{108} \begin{bmatrix} 22I_3 & 7I_3 & 7I_3 \\ 7I_3 & 22I_3 & 7I_3 \\ 7I_3 & 7I_3 & 22I_3 \end{bmatrix} \tag{A.8}$$

The matrix $\overline{H}^{(e)}$ can be conveniently lumped, obtaining:

$$\widetilde{H}^{(e)} = \frac{A^{(e)}}{3} I_9 \tag{A.9}$$

The use of $\widetilde{H}^{(e)}$ instead of $\overline{H}^{(e)}$ in the computation of $C^{(e)}$ is equivalent to assuming $N_u^{(e)} = N_\lambda^{(e)}$, i.e., using the same piecewise constant basis functions for both displacements and strengths on the IEs.

The local contribution $E^{(e)}$ can be derived from the global definition of $E(\mathbf{u}, \boldsymbol{\lambda})$ provided in equation (27). The first factor in the integral, i.e., $(c - \tan\varphi \mathbf{n}^{(e),T} N_\lambda^{(e)} R^{(e)} \boldsymbol{\lambda}^{(e)})$, is actually the value of the limiting shear strength $\tau_L^{(e)}$ computed at the elemental level:

$$\tau_L^{(e)} = \phi_i^{(e)} (\mathbf{x}) \tau_{L,i} + \phi_j^{(e)} (\mathbf{x}) \tau_{L,j} + \phi_k^{(e)} (\mathbf{x}) \tau_{L,k} \tag{A.10}$$

where $\tau_{L,m}$ is the limiting shear strength value at the nodes $m^{(1)}$ and $m^{(2)}$. The H-energy norm of $\mathbf{u}^{(e)}$ reads:

$$\left\| \mathbf{u}^{(e)} \right\|_H = \sqrt{\mathbf{u}^{(e),T} S^{(e),T} N_u^{(e),T} N_u^{(e)} S^{(e)} \mathbf{u}^{(e)}} = \sqrt{\mathbf{u}_r^{h,(e),T} \mathbf{u}_r^{h,(e)}} = \left\| \mathbf{u}_r^{h,(e)} \right\|_2 \tag{A.11}$$

Using equations (A.10) and (A.11), $E^{(e)}$ is obtained as:

$$E^{(e)} = S^{(e),T} \left[\int_{A^{(e)}} \tau_L^{(e)} \frac{\|\mathbf{u}_r^{h,(e)}\|_2^2 N_u^{(e),T} N_u^{(e)} - N_u^{(e),T} \mathbf{u}_r^{h,(e)} \mathbf{u}_r^{h,(e),T} N_u^{(e)}}{\|\mathbf{u}_r^{h,(e)}\|_2^3} dS \right] S^{(e)} \tag{A.12}$$

The integral in equation (A.12) has to be evaluated numerically. However, the computation of $E^{(e)}$ becomes straightforward using the assumption that leads to the lumped matrix $\widetilde{H}^{(e)}$ of equation (A.9), i.e., $N_u^{(e)} = N_\lambda^{(e)}$ on the IEs. In this case, equation (A.12) reads:

$$E^{(e)} = \frac{A^{(e)}}{3} S^{(e),T} \begin{bmatrix} \tau_{L,i} \frac{Q_i}{\|\mathbf{u}_{r,i}\|_2^3} & 0 & 0 \\ 0 & \tau_{L,j} \frac{Q_j}{\|\mathbf{u}_{r,j}\|_2^3} & 0 \\ 0 & 0 & \tau_{L,k} \frac{Q_k}{\|\mathbf{u}_{r,k}\|_2^3} \end{bmatrix} S^{(e)} \tag{A.13}$$

where Q_m is the 3×3 matrix:

$$Q_m = \left\| \mathbf{u}_{r,m} \right\|_2^2 I_3 - \mathbf{u}_{r,m} \mathbf{u}_{r,m}^T \tag{A.14}$$

The following useful result can be proved for the global matrix E.

Proposition. *The matrix E obtained by assembling the local contributions $E^{(e)}$ defined as in equation (A.13) is symmetric positive semi-definite.*

Proof. The matrix $E^{(e)}$ is symmetric by construction and its eigenvalues are those of the matrices:

$$\frac{A^{(e)} \tau_{L,m}}{3 \left\| \mathbf{u}_{r,m} \right\|_2^3} Q_m, \qquad m = i, j, k \tag{A.15}$$

Recalling equation (A.14), the eigenvalues μ of Q_m are computed as:

$$\det \left(\left\| \mathbf{u}_{r,m} \right\|_2^2 I_3 - \mathbf{u}_{r,m} \mathbf{u}_{r,m}^T - \mu I_3 \right) = \det \left(-\mathbf{u}_{r,m} \mathbf{u}_{r,m}^T - \chi I_3 \right) = 0 \tag{A.16}$$

with $\chi = \mu - \left\| \mathbf{u}_{r,m} \right\|_2^2$. The eigenvalues of the rank-one matrix $-\mathbf{u}_{r,m} \mathbf{u}_{r,m}^T$ are $\chi = \{ -\left\| \mathbf{u}_{r,m} \right\|_2^2, 0, 0 \}$, hence $\mu = \{ 0, \left\| \mathbf{u}_{r,m} \right\|_2^2, \left\| \mathbf{u}_{r,m} \right\|_2^2 \}$ and the eigenvalues of $E^{(e)}$ are either positive or zero. $\square$

Therefore, if the stiffness matrix K of the discretized 3D body is symmetric positive definite, the $(1,1)$ block (27) of the Jacobian is also so.

Finally, the contribution $F^{(e)}$ is computed by writing at the elemental level the global definition of $F(\mathbf{u})$ in equation (30). The matrix $N_{n,\lambda}^{(e)} = \mathbf{n}^{(e),T} N_\lambda^{(e)} R^{(e)}$ selects from the local vector $\boldsymbol{\lambda}^{(e)}$ the components $\lambda_{\zeta,m}$ of the normal strength for each pair of nodes $m = i, j, k$ of the IE e. Hence, $N_{n,\lambda}^{(e)}$ is actually the first row of $N_\lambda^{(e)}$ in equation (A.4):

$$N_{n,\lambda}^{(e)}(\mathbf{x}) = \left[\begin{array}{ccccccccc} \phi_i^{(e)}(\mathbf{x}) & 0 & 0 & \phi_j^{(e)}(\mathbf{x}) & 0 & 0 & \phi_k^{(e)}(\mathbf{x}) & 0 & 0 \end{array} \right] \tag{A.17}$$

Recalling equation (A.11) and using the definition (A.17), $F^{(e)}$ can be computed as:

$$F^{(e)} = S^{(e),T} \int_{A^{(e)}} \tan\varphi \, \frac{N_u^{(e),T} N_u^{(e)} \mathbf{u}_r^{(e)}}{\left\| \mathbf{u}_r^{h,(e)} \right\|_2} N_{n,\lambda}^{(e)} \, dS \tag{A.18}$$

Similarly to $E^{(e)}$, the integral in equation (A.18) has to be evaluated numerically. However, assuming $N_u^{(e)} = N_\lambda^{(e)}$ on the IEs allows for a straightforward computation of $F^{(e)}$. Approximating φ at the elemental level as:

$$\varphi^{(e)} = \phi_i^{(e)}(\mathbf{x}) \varphi_i + \phi_j^{(e)}(\mathbf{x}) \varphi_j + \phi_k^{(e)}(\mathbf{x}) \varphi_k \tag{A.19}$$

where φ_m is the friction angle at the pair of nodes $m^{(1)}$ and $m^{(2)}$, $F^{(e)}$ reads:

$$F^{(e)} = \frac{A^{(e)}}{3} S^{(e),T} \begin{bmatrix} \tan\varphi_i \frac{\mathbf{u}_{r,i}}{\|\mathbf{u}_{r,i}\|_2} & 0 & 0 & 0 & 0 & 0 & 0 & 0 & 0 \\ 0 & 0 & 0 & \tan\varphi_j \frac{\mathbf{u}_{r,j}}{\|\mathbf{u}_{r,j}\|_2} & 0 & 0 & 0 & 0 & 0 \\ 0 & 0 & 0 & 0 & 0 & 0 & \tan\varphi_k \frac{\mathbf{u}_{r,k}}{\|\mathbf{u}_{r,k}\|_2} & 0 & 0 \end{bmatrix} \tag{A.20}$$

References

[1] D.L. Galloway, T.J. Burbey, Review: regional land subsidence accompanying groundwater extraction, Hydrogeol. J. 19 (2011) 1459–1486.

[2] G. Gambolati, P. Teatini, Geomechanics of subsurface water withdrawal and injection, Water Resour. Res. 51 (2015) 3922–3955.

[3] M. Ferronato, G. Gambolati, C. Janna, P. Teatini, Numerical modelling of regional faults in land subsidence prediction above gas/oil reservoirs, Int. J. Numer. Anal. Methods Geomech. 32 (2008) 633–657.

[4] J. Rutqvist, C.F. Tsang, A study of caprock hydromechanical changes associated with CO_2-injection into a brine formation, Environ. Geol. 42 (2002) 296–305.

[5] J.T. Birkholzer, Q. Zhou, Basin-scale hydrogeologic impacts of CO_2 storage: capacity and regulatory implications, Int. J. Greenh. Gas Control 3 (2009) 745–756.

[6] M. Ferronato, G. Gambolati, C. Janna, P. Teatini, Geomechanical issues of anthropogenic CO_2 sequestration in exploited gas fields, Energy Convers. Manag. 51 (2010) 1918–1928.

[7] P. Teatini, N. Castelletto, G. Gambolati, 3D geomechanical modeling for CO_2 geological storage in faulted formations. A case study in an offshore northern Adriatic reservoir, Italy, Int. J. Greenh. Gas Control 22 (2014) 63–76.

[8] P. Teatini, N. Castelletto, M. Ferronato, G. Gambolati, C. Janna, E. Cairo, D. Marzorati, D. Colombo, A. Ferretti, A. Bagliani, F. Bottazzi, Geomechanical response to seasonal gas storage in depleted reservoirs: a case study in the Po river basin, Italy, J. Geophys. Res. 116 (2011) B08407, http://dx.doi.org/10.1029/2010JB008122.

[9] N. Castelletto, M. Ferronato, G. Gambolati, C. Janna, D. Marzorati, P. Teatini, Can natural fluid pore pressure be safely exceeded in storing gas underground?, Eng. Geol. 153 (2013) 35–44.

[10] J.T. Fredrich, J.G. Arguello, G.L. Deitrick, E.P. de Rouffignac, Geomechanical modeling of reservoir compaction, surface subsidence, and casing damage at the Belridge diatomite field, SPE Reserv. Eval. Eng. 3 (2000) 348–359.

[11] N. Castelletto, M. Ferronato, G. Gambolati, C. Janna, P. Teatini, Numerical modelling of case sliding in radioactive marker boreholes of the Northern Adriatic basin, Italy, SPE Reserv. Eval. Eng. 13 (2010) 906–913.

[12] P.J. Gonzalez, K.F. Tiampo, M. Palano, F. Cannavo, J. Fernandez, The 2011 Lorca earthquake slip distribution controlled by groundwater crustal unloading, Nat. Geosci. 5 (2011) 821–825.

[13] E.E. Brodsky, L.J. Lajoie, Anthropogenic seismicity rates and operational parameters at the Salton Sea geothermal field, Science 341 (2013) 543–546.

[14] X. Lei, S. Ma, W. Cheng, C. Pang, J. Zeng, B. Jiang, A detailed view of the injection-induced seismicity in a natural gas reservoir in Zigong, southwestern Sichuan Basin, China, J. Geophys. Res., Solid Earth 118 (2013) 4296–4311.

[15] K.M. Keranen, H.M. Savage, G.A. Abers, E.S. Cochran, Potentially induced earthquakes in Oklahoma, USA: links between wastewater injection and the 2011 M_w 5.7 earthquake sequence, Geology 41 (2013) 699–702.

[16] N.J. van der Elst, H.M. Savage, K.M. Keranen, G.A. Abers, Enhanced remote earthquake triggering at fluid-injection sites in the midwestern United States, Science 341 (2013) 164–167.

[17] T. Engelder, Capillary tension and imbibition sequester frack fluid in Marcellus gas shale, Proc. Natl. Acad. Sci. USA 109 (2012) E3625.

[18] N.R. Warner, R.B. Jackson, T.H. Darrah, S.G. Osborn, A. Down, K. Zhao, A. White, A. Vengosh, Reply to Engelder: potential for fluid migration of Marcellus Formation remains possible, Proc. Natl. Acad. Sci. USA 109 (2012) E3626.

[19] L. Cueto-Felgueroso, R. Juanes, Forecasting long-term gas production from shale, Proc. Natl. Acad. Sci. USA 110 (2013) 660–661.

[20] T.L. Holzer, S.N. Davis, B.E. Lofgren, Faulting caused by groundwater extraction in southcentral Arizona, J. Geophys. Res. 84 (1979) 603–612.

[21] L. Rothenburg, A. Obha, A. El Baruni, Horizontal ground movements due to water abstraction and formation of earth fissures, in: F.B.J. Barends, et al. (Eds.), Land Subsidence, in: IAHS Publ., vol. 234, IAHS Press, Wallingford, UK, 1995, pp. 239–249.

[22] D.Y. Geng, Z.S. Li, Ground fissure hazards in USA and China, Acta Seismol. Sin. 13 (2000) 466–476.

[23] D. Carreon-Freyre, M. Cerca, M. Hernandez-Marin, Propagation of fracturing related to land subsidence in the Valley of Queretaro, Mexico, in: A. Zhang, et al. (Eds.), Proceedings of the Seventh International Symposium on Land Subsidence, vol. 1, Shanghai Scientific & Technical Publ., China, 2005, pp. 155–164.

[24] J. Rutqvist, J.T. Birkholzer, C.F. Tsang, Coupled reservoir-geomechanical analysis of the potential for tensile and shear failure associated with CO_2 injection in multilayered reservoir-caprock systems, Int. J. Rock Mech. Min. Sci. 45 (2008) 132–143.

[25] F. Cappa, J. Rutqvist, Impact of CO_2 geological sequestration on the nucleation of earthquakes, Geophys. Res. Lett. 38 (2011) L17313, http://dx.doi.org/10.1029/2011GL048487.

[26] F. Cappa, J. Rutqvist, Modeling of coupled deformation and permeability evolution during fault reactivation induced by deep underground injection of CO_2, Int. J. Greenh. Gas Control 5 (2011) 336–346.

[27] H. Kanamori, D.L. Anderson, Theoretical basis of some empirical relations in seismology, Bull. Seismol. Soc. Am. 65 (1975) 1073–1095.

[28] A. Mazzoldi, A.P. Rinaldi, A. Borgia, J. Rutqvist, Induced seismicity within geological carbon sequestration projects: maximum earthquake magnitude and leakage potential from undetected faults, Int. J. Greenh. Gas Control 10 (2012) 434–442.

[29] R.E. Goodman, R.L. Taylor, T.L. Brekke, A model for the mechanics of jointed rock, J. Soil Mech. Found. Div. 94 (1968) 637–659.

[30] G. Beer, An isoparametric joint/interface element for finite element analysis, Int. J. Numer. Methods Eng. 21 (1985) 585–600.

[31] S. Cescotto, R. Charlier, Frictional contact finite elements based on mixed variational principles, Int. J. Numer. Methods Eng. 36 (1993) 1681–1701.

[32] R. Juanes, J. Samper, J. Molinero, A general and efficient formulation of fractures and boundary conditions in the finite element method, Int. J. Numer. Methods Eng. 54 (2002) 1751–1774.

[33] B.T. Aagaard, M.G. Knepley, C.A. Williams, A domain decomposition approach to implementing fault slip in finite-element models of quasi-static and dynamic crustal deformation, J. Geophys. Res., Solid Earth 118 (2013) 3059–3079.

[34] B. Jha, R. Juanes, Coupled multiphase flow and poromechanics: a computational model of pore pressure effects on fault slip and earthquake triggering, Water Resour. Res. 50 (2014) 3776–3808.

[35] M. Ferronato, C. Janna, G. Gambolati, Mixed constraint preconditioning in computational contact mechanics, Comput. Methods Appl. Mech. Eng. 197 (2008) 3922–3931.

[36] C. Janna, M. Ferronato, G. Gambolati, Multilevel incomplete factorizations for the iterative solution of non-linear FE problems, Int. J. Numer. Methods Eng. 80 (2009) 651–670.

[37] M. Ferronato, C. Janna, G. Pini, Parallel solution to ill-conditioned FE geomechanical problems, Int. J. Numer. Anal. Methods Geomech. 36 (2012) 422–437.

[38] D.P. Bertsekas, Constrained Optimization and Lagrange Multiplier Methods, Academic Press, New York, 1984.

[39] J.C. Simo, T.J.R. Hughes, Computational Inelasticity, Springer, New York, 2000.

[40] P. Wriggers, Contact Mechanics, Springer, Berlin, 2005.

[41] P. Wriggers, G. Zavarise, Computational contact mechanics, in: E. Stein, R. de Borst, T.J.R. Hughes (Eds.), Encyclopedia of Computational Mechanics, vol. 2, John Wiley & Sons, 2004, pp. 195–226.

[42] J.C. Jaeger, N.G.W. Cook, Fundamentals of Rock Mechanics, Chapman & Hall, London, 1979.

[43] J.H. Dieterich, Modeling of rock friction: 1. Experimental results and constitutive equations, J. Geophys. Res. 84 (1979) 2161–2168.

[44] A.L. Ruina, Slip instability and state variable friction laws, J. Geophys. Res. 88 (1983) 10359–10370.

[45] C. Marone, Laboratory-derived friction laws and their application to seismic faulting, Annu. Rev. Earth Planet. Sci. 26 (1998) 643–696.

[46] O.C. Zienkiewicz, R.L. Taylor, The Finite Element Method, Butterworth–Heinemann, Oxford, 2000.

[47] M. Benzi, G.H. Golub, J. Liesen, Numerical solution of saddle point problems, Acta Numer. 14 (2003) 1–137.

[48] A.V. Phan, J.A.L. Napier, L.J. Gray, T. Kaplan, Symmetric-Galerkin BEM simulation of fracture with frictional contact, Int. J. Numer. Methods Eng. 57 (2003) 835–851.

[49] C. Janna, M. Ferronato, G. Gambolati, P. Teatini, Simulation of ground failure due to groundwater pumping, in: Land Subsidence, Associated Hazards and the Role of Natural Resources Development, in: IAHS Publ., vol. 339, 2010, pp. 133–135.